J Phys IV France **12** (2002)
© EDP Sciences, Les Ulis
DOI 10 1051/jp4 20020327

Tensile properties and microstructure of 9Cr-1Mo martensitic steels containing a high helium concentration

J. Henry, P. Jung[1], J. Chen[1] and J.-C. Brachet

CEA/Saclay, Service de Recherches Métallurgiques Appliquées, 91191 Gif-sur-Yvette cedex, France
[1] *Institut für Festkörperforschung, Forschungszentrum Jülich, 52425 Jülich, Germany*

Abstract - Tensile tests and microstructural examinations were performed on 100 μm thick specimens of 9Cr-1Mo (EM10) and modified 9Cr-1Mo (T91) martensitic steels homogeneously implanted with 23 MeV α particles to a concentration of 5000 appm. Two implantation temperatures were selected, 250 and 550°C, which correspond respectively to the lower (higher) bound of the operation temperature range foreseen for the window of Accelerator Driven Systems devoted to waste transmutation. 250°C is also the maximum operating temperature of the ESS (European Spallation Source) window. The specimens were tested at room and implantation temperatures and the fracture surfaces were characterized using scanning electron microscopy. It was found that implantation at 250°C induces a very strong hardening of both materials together with a total loss of ductility. Embrittlement was also observed for the specimens implanted at 550°C, however the ductility loss was much less severe. Preliminary Transmission Electron Microscopy (TEM) observations are presented. Helium bubbles were observed in the specimens implanted at 550°C but none could be detected in the samples implanted at the lower temperature. However, based on results of Small Angle Neutron Scattering experiments performed on samples implanted together with the tensile specimens, it is proposed that the high degree of hardening following implantation at 250°C is due to the formation of a high density of tiny helium bubbles. It is furthermore suggested that the brittle, intergranular fracture mode displayed by these specimens results from the combined effects of pronounced intragranular hardening and weakening of Prior Austenite Grain (PAG) boundaries due to helium.

Résumé – Propriétés de traction et microstructure d'aciers martensitiques 9Cr-1Mo contenant une forte concentration d'hélium. Des essais de traction et des examens microstructuraux ont été effectués sur des éprouvettes en aciers martensitiques 9Cr-1Mo (EM10) et 9Cr-1MoVNb (T91) de 100 μm d'épaisseur, implantées de façon homogène en hélium jusqu'à une teneur de 5000 ppm at. Deux températures d'implantation ont été choisies : 250 et 550°C qui correspondent respectivement à la borne basse et haute du domaine de température de fonctionnement actuellement envisagé pour un démonstrateur de réacteur hybride dédié à la transmutation de déchets radioactifs. 250°C est également la température maximale de fonctionnement de la fenêtre de la source ESS (European Spallation Source). Les essais de traction ont été réalisés à température ambiante ainsi qu'à la température d'implantation et une

caractérisation des faciès de rupture a été effectuée par Microscopie Electronique à Balayage. Il a été constaté que l'implantation d'hélium à 250°C induit un durcissement très important associé à une perte totale de ductilité. Une fragilisation est également mise en évidence à 550°C, mais les échantillons conservent néanmoins une certaine ductilité. Des résultats préliminaires d'observations par Microscopie Electronique en Transmission (MET) sont présentés. Des bulles d'hélium sont observées dans les échantillons implantés à 550°C, mais la présence de bulles n'a pas pu être détectée dans les échantillons implantés à plus basse température. Néanmoins, sur la base de résultats d'expériences de Diffusion de Neutrons aux Petits Angles effectuées récemment sur des échantillons implantés dans les mêmes conditions que les éprouvettes de traction, nous pensons que le très fort durcissement induit par l'implantation à 250°C est dû à la formation d'une densité élevée de petites bulles d'hélium. Nous suggérons par ailleurs que le mode de rupture fragile et intergranulaire observé après implantation à 250°C est le résultat des effets combinés du durcissement et d'une diminution de l'énergie de cohésion au niveau des joints de grain induite par la présence d'hélium.

1. INTRODUCTION

Liquid metal spallation targets will be used in different facilities currently being planned such as ADS (accelerator driven systems) devoted to the transmutation of radioactive wastes or neutron sources dedicated to research in materials science and condensed matter physics (for instance the European Spallation Source, ESS). The structural materials of high power liquid metal targets, and primarily the proton beam window, will be exposed to intense fluxes of high energy protons and neutrons generating both high levels of radiation damage (typically several tens of dpa after one year of operation) but also significant quantities of impurities produced by spallation reactions occurring inside the window material

Among these, helium is of particular concern : this element has a high production rate and the quantities accumulated in the window within one year could reach up to 1 at % as in the case of ESS [1]. He effects on mechanical properties of austenitic and martensitic stainless steels have been investigated in the past, especially as part of materials research activities for the fusion technology programme. High temperature helium embrittlement, a phenomenon which typically occurs at temperatures higher than 0.45 T_m (where T_m is the melting temperature) and consists in reduced rupture times in creep tests due to helium bubble formation at grain boundaries, received for instance considerable attention [2]. It was shown in particular that martensitic steels have a superior resistance to this specific He effect compared to austenitic steels. However, experimental results pertaining to helium effects at low temperature and more generally data relative to the very high helium concentrations reached in the window are scarce We report here results of tensile tests and microstructural investigations carried out on 9Cr-1 Mo (EM10) and 9 Cr-1 Mo VNb (T91) martensitic steels implanted with 0.5 at % He at 250 and 550°C. Both steels are candidate materials for the proton beam window of ADS and T91 was selected as material for the window of the 1 MW MEGAPIE target [3].

2. EXPERIMENTAL

2.1. Specimen preparation

The chemical compositions of the two martensitic steels used in this study are given in *table I*. Sheets about 100 µm in thickness were obtained by cold rolling from 0.5 mm plates. Tensile specimens of overall dimensions 28 x 8 x 0.1 mm with 12 x 2 mm gauge section were cut by spark erosion and subsequently submitted to the following normalisation and tempering conditions . 15 min at 970°C followed by 30 mn at 750°C for EM10 and 1 hr at 1050°C plus 1 hr at 760°C for T91.

Prior austenite grain size measurements showed a broad size distribution with average values of 21 μm in the case of EM10 and 14 μm for T91.

Table I. Chemical compositions of the materials (in weight %).

Steel	C	Cr	Mo	V	Nb	Ni	Mn	N	P	Si
EM10	0 096	8.8	1.09	-	-	0.18	0.51	0.024	0 015	0.37
T91	0.105	8.26	0.95	0.2	0.075	0.13	0.38	0.0055	0 009	0.43

2.2. Helium implantation

Four tensile specimens were mounted on one holder for implantation. The specimens were fixed on one end with the other end free in order to avoid stresses from thermal expansion. The specimens had mutual separations of 1 mm and implantation was extended over a length of 13 mm. This ensured implantation also in the fillets up to the grip region for tensile testing. The two central specimens were offset in beam direction with respect to the outer ones to obtain equal cooling for all specimens. The specimens were heated by the beam current while cooling was supplied by flowing helium gas which passes the specimens tangentially from both sides at velocities up to 100 m/s. The gas entered the apparatus through ten adjustable nozzles and was continuously cleaned in a cooling circuit [4, 5]. Temperature was adjusted by the flow rate of the gas. One specimen was electrically insulated by Kapton foils to allow determination of average temperature along the gauge length by measurement of electrical resistivity with a current of 0.1 A. Heating by this current was negligible. Relative temperature measurement was performed by a movable infrared pyrometer directed towards the specimens at an angle of 45° with a measuring spot of about 1 mm in diameter. To obtain conditions as similar as possible for all specimens, the inner and outer specimens were exchanged after half the total dose.

The holders were mounted in an irradiation apparatus at a beam line of the Jülich Compact Cyclotron. The α-beam of energy 27 4 MeV (as measured by an inductive method) passed through a 13 x 13 mm aperture and a 28 μm Hastelloy window. In order to achieve uniform implantation, the energy of the beam, equal to 22.8 MeV behind the window, was furthermore variably degraded by a rotating wheel made of 24 aluminium foils of different thicknesses. The calculated deviation from homogeneous implantation is less than 1 % [6]. For the sake of homogeneity, the beam was scanned at sawtooth frequencies of typically 300 Hz in both directions across the specimens. The beam could be stopped by a shutter, which was also used for electrical measurement of the beam current. Electrical measurement of the beam current in the apparatus during implantation was not possible due to ionisation of the cooling gas. Calibration of implanted helium concentration was derived previously from helium desorption experiments [7], giving a correction factor of about 0.7 to the calculation from beam current, which is ascribed to the emission of secondary electrons from the shutter.

At 250°C, the implantation rate was limited by the available cooling power. In this case a pressure of the flowing helium gas of about 1 bar was applied, giving a typical flow velocity of 100 m/s and an implantation rate of 15 at ppb/s. On the other hand, at 550°C, the implantation rate was limited by the available beam current The helium pressure was reduced to typically 0.6 bar and the implantation rate was increased to typically 20 at ppb/s.

Using the Monte-Carlo SRIM code [21] and a displacement energy threshold of 40 eV, the damage induced by the irradiation with the degraded 22.8 MeV beam of α particles was calculated to be 148 displacements per implanted helium atom. For an implanted helium concentration of 0.5 at%, the irradiation dose is therefore about 0.7 dpa.

2.3. Tensile tests and microstructural characterisation

Specimens were mounted in a tensile apparatus for miniature specimens, situated in a vacuum furnace at pressures below 10^{-5} Pa. Tensile tests were carried out at room and implantation temperatures. Relative strain rates were around 10^{-4}/s. Strains were calculated from length change divided by the effective gauge length (11 mm)

After testing, fracture surface characterisation was performed by Scanning Electron Microscopy (using either a Hitachi-F800 or a JEOL 6004 operated at 20 kV and 15 kV, respectively).

Discs (2 mm in diameter) were subsequently punched out from the gauge section of the tensile specimens and thin foils were prepared by jet electropolishing. Implantation microstructure was examined using two transmission electron microscopes: a JEOL 2010 F (200 kV) and a Philipps EM430 (300 kV).

3. RESULTS

3.1. Tensile tests

Figures 1-4 show stress-strain curves of implanted and unimplanted tensile specimens tested at 25, 250 or 550°C.

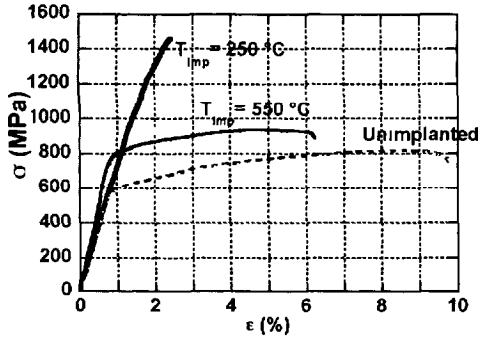

Figure 1. Stress-strain curves of EM10 implanted with 0.5 at % He at 250 and 550°C. The dotted line corresponds to the unimplanted reference specimen Tensile tests were performed at 25°C.

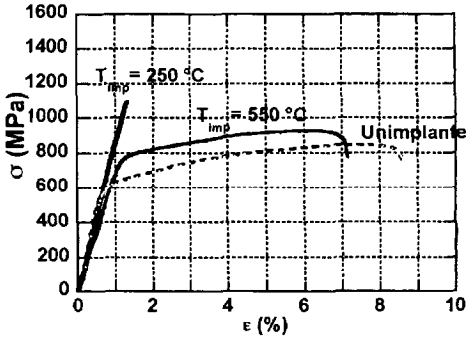

Figure 2. Stress-strain curves of T91 implanted with 0 5 at % He at 250 and 550°C. Tensile tests were performed at 25°C.

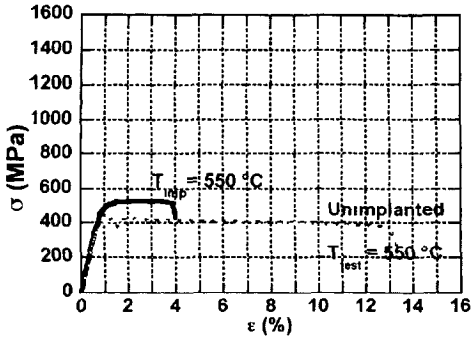

Figure 3. Stress-strain curves of EM10 implanted with 0.5 at % He at 550°C Tensile tests were performed at 550°C.

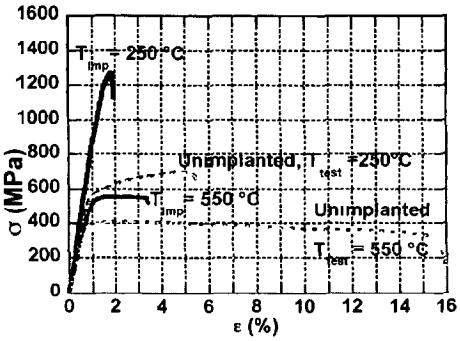

Figure 4. Stress-strain curves of T91 implanted with 0.5 at % He at 250 and 550°C. Tensile tests were performed at the implantation temperature.

Both EM10 and T91 specimens implanted at 250°C and tested at room temperature broke in the fillets. All other specimens broke in the gauge section. It must be pointed out that the first specimen (EM10 sample implanted at 250°C) was so brittle that it broke before mounting (this problem was avoided on subsequent specimens by extreme care during mounting). As a result, the second EM10 specimen implanted at 250°C was tested at room temperature and testing at 250°C was not carried out (see *figure 3*). It can be seen from *figures 1* and *2* that both specimens implanted at 250°C and tested at room temperature did not show any sign of plastic deformation (as confirmed by SEM observations, see below). Furthermore, implantation-induced hardening is very high. A lesser amount of hardening is also observed in the case of the EM10 and T91 specimens implanted at 550°C and in this case some plastic deformation occured before fracture T91 implanted and tested at 250°C (*figure 4*) experienced some plastic deformation but fracture occured with a much reduced total elongation with respect to the unimplanted case. Moreover, a very strong yield stress increase following implantation is observed.

Finally, an overall picture of the decrease of ductility as a function of implantation and testing conditions is given in *figure 5* which shows the values of reduction of area for implanted and unimplanted samples.

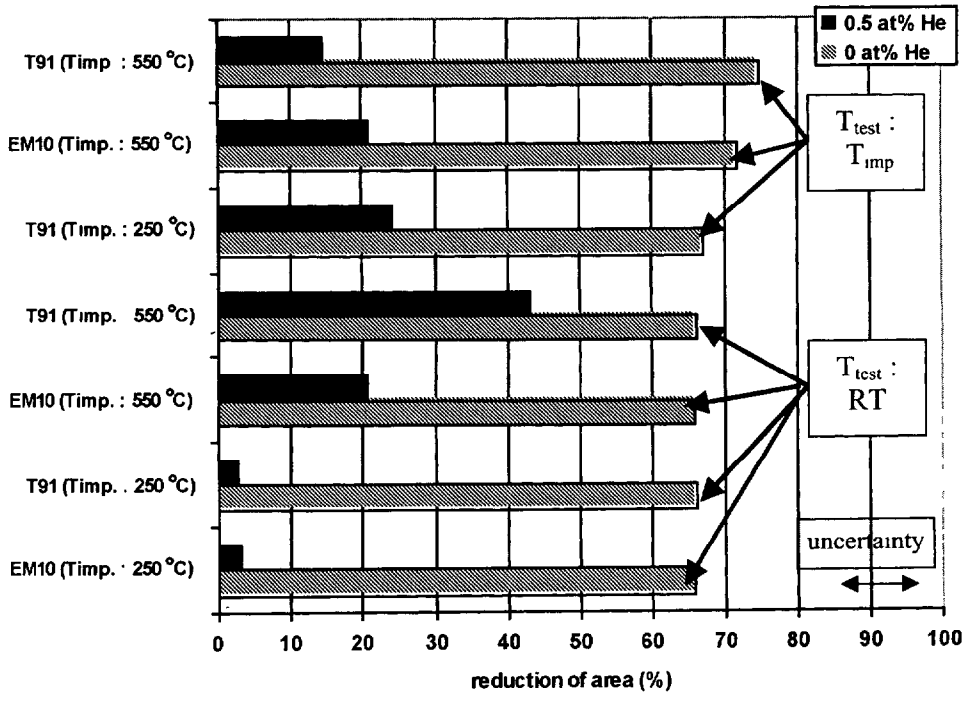

Figure 5. Relative reduction of area (z) of unimplanted and implanted tensile specimens. The parameter z is defined as : $z = 1\text{-}w_{neck}/d$, where w_{neck} is the width of the neck (measured using SEM as described below) and d is the initial width of the specimen Uncertainty on RA values is estimated to be ± 5 %.

3.2. SEM observations

Characterisation of fracture surfaces using SEM was carried out following tensile testing. *Figures 6-7* show low magnification images of unimplanted EM10 and T91 specimens tested at room temperature.

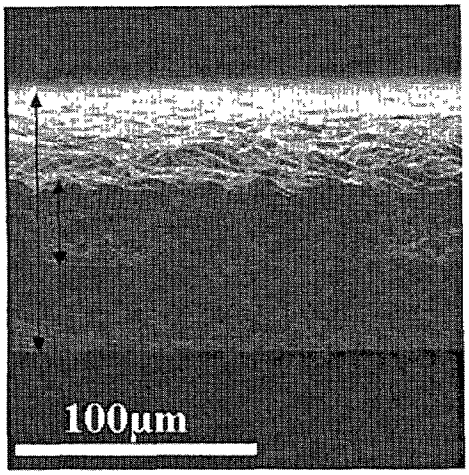

Figure 6. SEM micrograph showing the fracture surface of an unimplanted EM10 tensile specimen tested at 25°C. The short arrow indicates the width of the neck, to be compared to the width of the uniformly deformed section of the specimen (long arrow).

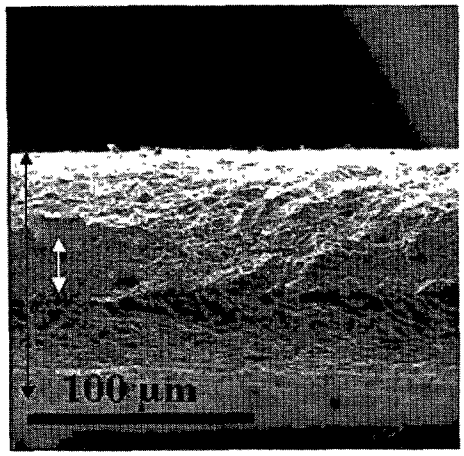

Figure 7. SEM micrograph of an unimplanted T91 specimen tested at 25°C.

In all unimplanted specimens the fracture mode was transgranular with a fully ductile fracture appearance of the type shown on *Figure 8*. Following implantation, the situation changed drastically, as can be seen on *Figures 9* and *10*. Both micrographs show clearly that T91 and EM10 specimens implanted with 0.5 at% He at 250°C and tested at room temperature broke without any necking. The predominantly intergranular fracture mode is also obvious. The fracture occurred along Prior Austenitic Grain boundaries (PAG). One can notice the difference in PAG sizes between EM10 (coarse grain structure, *Figure 10*) and T91 with a finer grain size (*Figure 9a*) due to the presence of niobium-rich carbonitrides which pin PAG during thermal treatment at high temperature.

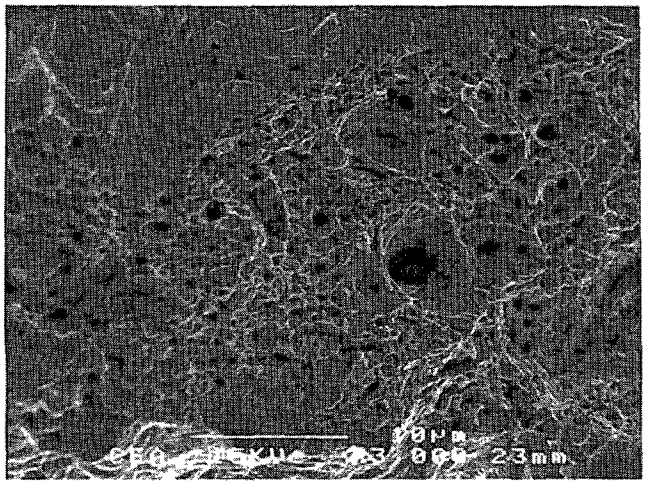

Figure 8. SEM micrograph showing ductile dimple fracture mode, typical of all unimplanted specimens. EM10 sample tested at 250°C.

Moreover, some areas with cleavage-like features can be found on the fracture surfaces of both EM10 and T91 specimens implanted at 250°C and tested at RT as shown for instance on *Figure 9c*

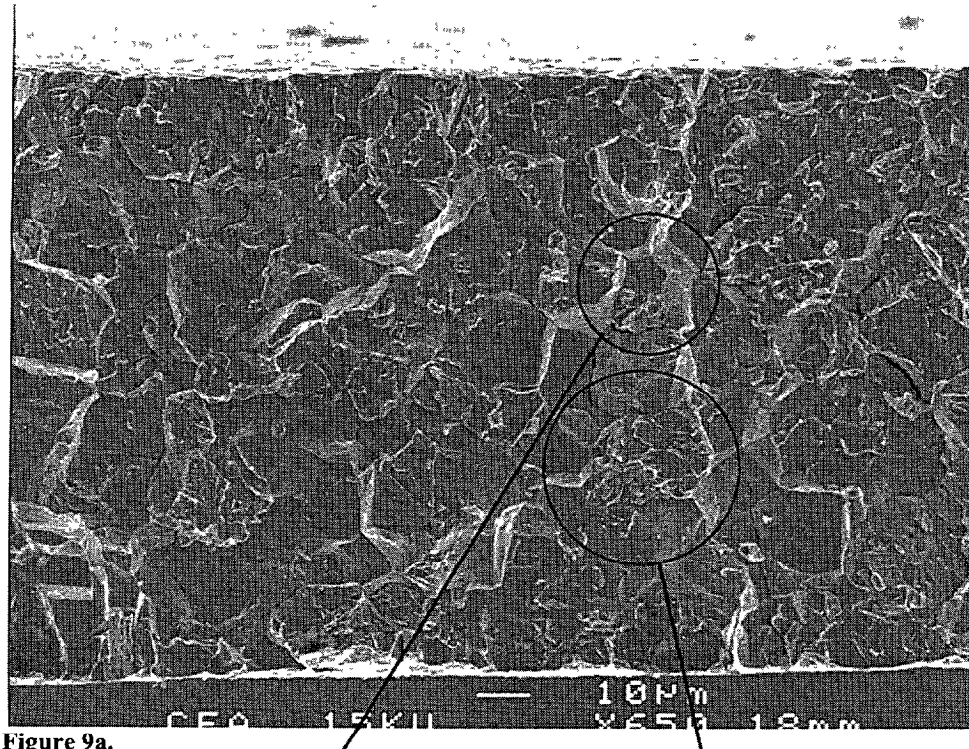

Figure 9a.

Figure 9b.

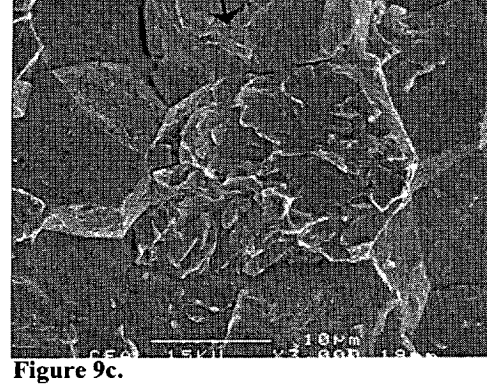

Figure 9c.

Figure 9. T91 sample implanted with 0.5 at% He at 250°C and tested at room temperature. Micrograph 9a presents a general view of the broken specimen. Micrographs 9b : detail of the predominantly intergranular fracture surface. Micrograph 9c : example of cleavage-like features.

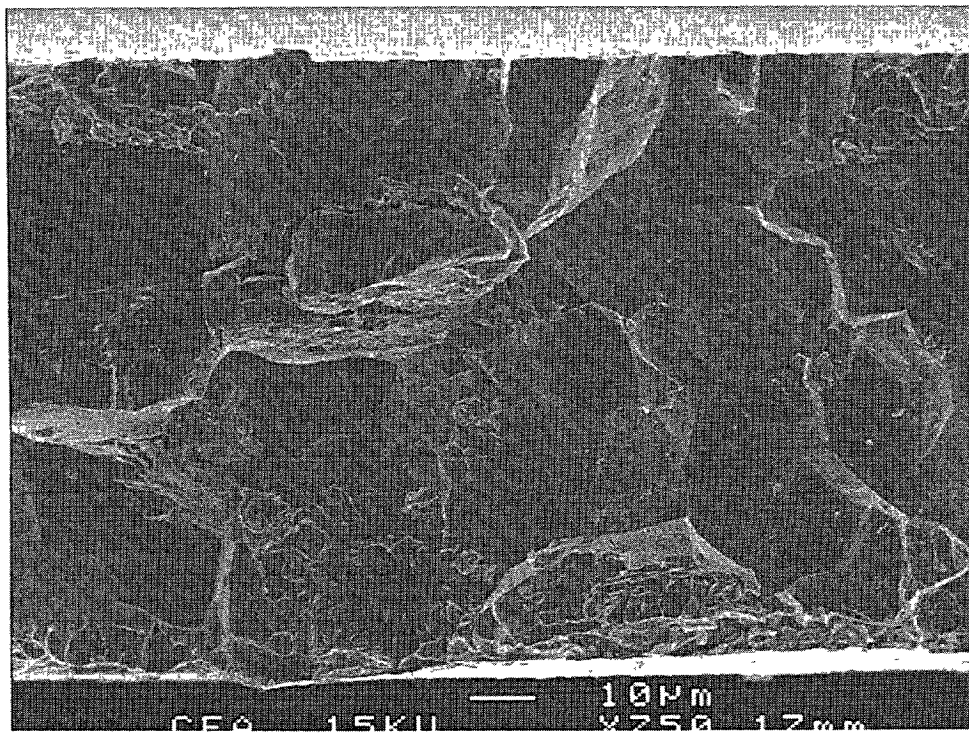

Figure 10. EM10 specimen implanted with 0.5 at% He at 250°C and tested at room temperature.

Following tensile testing at 250°C of the second T91 sample implanted at 250°C, the fracture mode is more complex One can clearly see on the image of the broken specimen (*Figure 11a*), that necking had begun prior to rupture, in accordance with the tensile curve (*Figure 4*). Fracture occured partly along the necking line, which makes an angle of approximately 60 ° with the specimen axis, as expected in a tensile test of a flat strip [10]. In this region of the fracture surface, the appearance is mixed : numerous intergranular facets are present (*Figure 11c*) but there is also indication of ductile failure mode (elongated dimples, *Figure 11d*) Such is not the case in the part of the specimen which broke perpendicular to the load axis : in this region, the fracture surface has a nearly fully intergranular appearance as shown on *Figure 11b*.

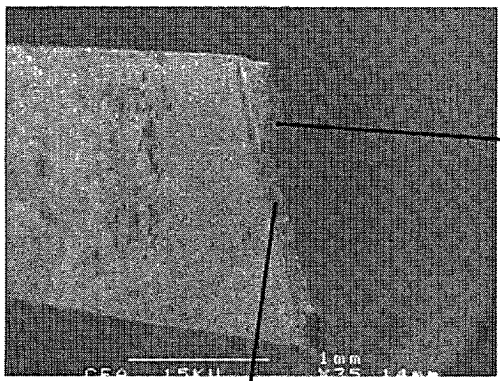

Fig. 11a.

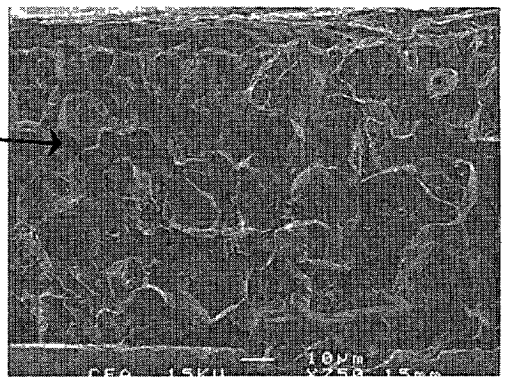

Fig. 11b.

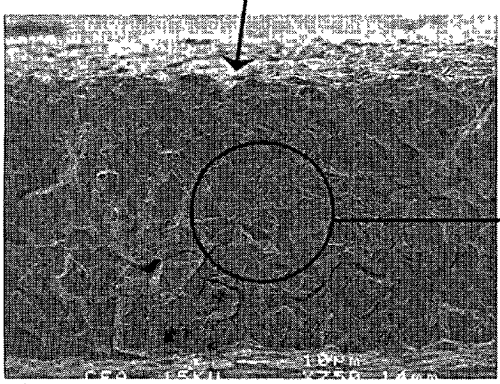

Fig 11c.

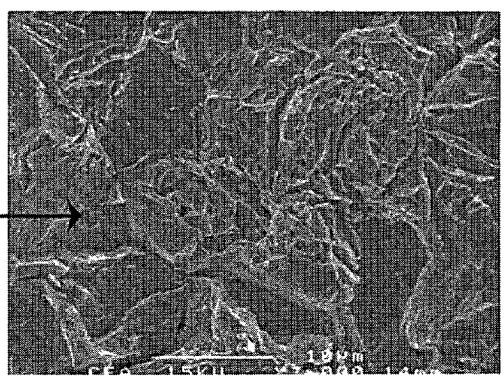

Fig 11d.

Figure 11. T91 tensile specimen implanted with 0.5 at% He at 250°C and tested at 250°C. Micrograph 11a: general view of the broken specimen. Micrograph 11b showing the fracture surface perpendicular to the load axis. Micrograph 11c: fracture surface along the necking line. Micrograph 11d: detail of micrograph 11c showing some elongated dimples.

After implantation at 550°C, some necking occurs at both testing temperatures, but ductility is significantly reduced in comparison with that of the unimplanted materials. Intergranular facets are seen after testing both at room temperature and at 550°C (an example is given in *figure 12*), but with a much rarer occurrence than after implantation and testing at 250°C. Ductile zones of the type shown on *figure 13* are observed. The flat appearance of the dimples is a further indication of the low overall ductility of the materials implanted at 550°C. Finally one has to point out that features with a "foliated" appearance were seen on the fracture surfaces of the steels implanted and tested at 550°C (*figure 14*). The fracture mechanism is not obvious (inter-lath decohesion?, quasi-cleavage?)

Figure 12. T91 tensile specimen implanted with 0.5 at% He at 550°C and tested at 550°C. Micrograph showing two grain boundaries, covered with globular particles (probably $M_{23}C_6$ carbides).

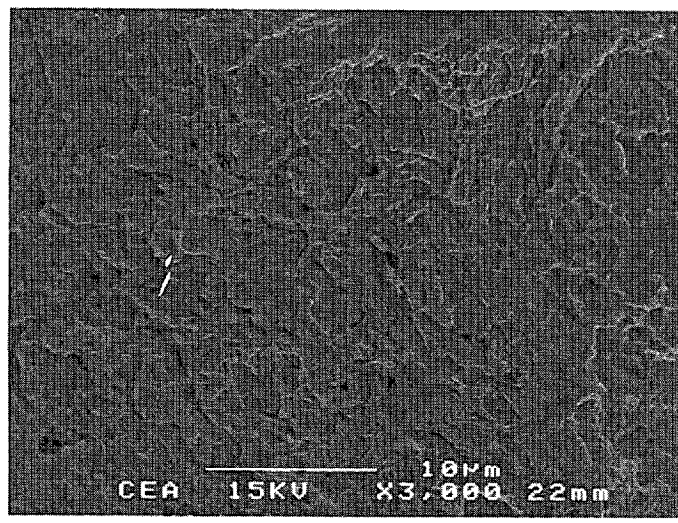

Figure 13. T91 tensile specimen implanted with 0.5 at% He at 550°C and tested at 550°C. Micrograph showing flat dimples.

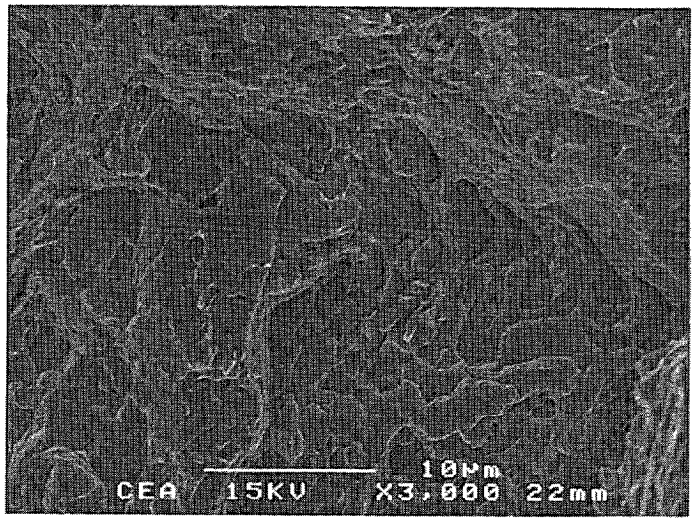

Figure 14. EM10 tensile specimen implanted with 0.5 at% He at 550°C and tested at 550°C. Micrograph showing "foliated" features seen on the fracture surface.

3.3. Microstructure

Preliminary TEM investigations of the microstructure were carried out : it was found that the microstructural features induced by the low temperature implantation differ markedly from those observed following implantation at 550°C. However, for a given implantation temperature, microstructures are very similar for both EM10 and T91.

3.3.1. Materials implanted at 250°C. TEM observations revealed that implantation-induced microstructures of EM10 and T91 implanted at 250°C consist of a high number density of small defect clusters, as shown on *figure 15*. We looked for the possible presence of Helium bubbles using over- and under-focus imaging conditions (Fresnel contrast). However, no bubbles were detected.

3.3.2. Materials implanted at 550°C By contrast, under defocused mode, bubbles were clearly seen in the steels implanted at 550°C. Bubble nucleation occurs preferentially on different microstructural features of the martensite : on dislocations inside the laths, on sub-grain, lath and PAG boundaries as well as on carbide-matrix interfaces (*figure 16*) While a fraction of the bubbles are approximately spherical, faceted bubbles are often seen as shown for instance on *figure 17*. Finally, it must also be pointed out that no point defect clusters are discerned after implantation at 550°C.

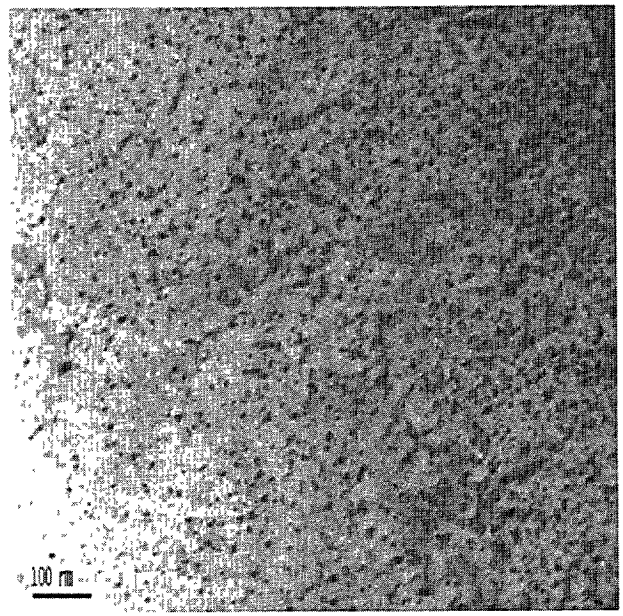

Figure 15. Bright field TEM micrograph showing small defect clusters, g = 110, s > 0 EM10 implanted with 0.5 at% He at 250°C.

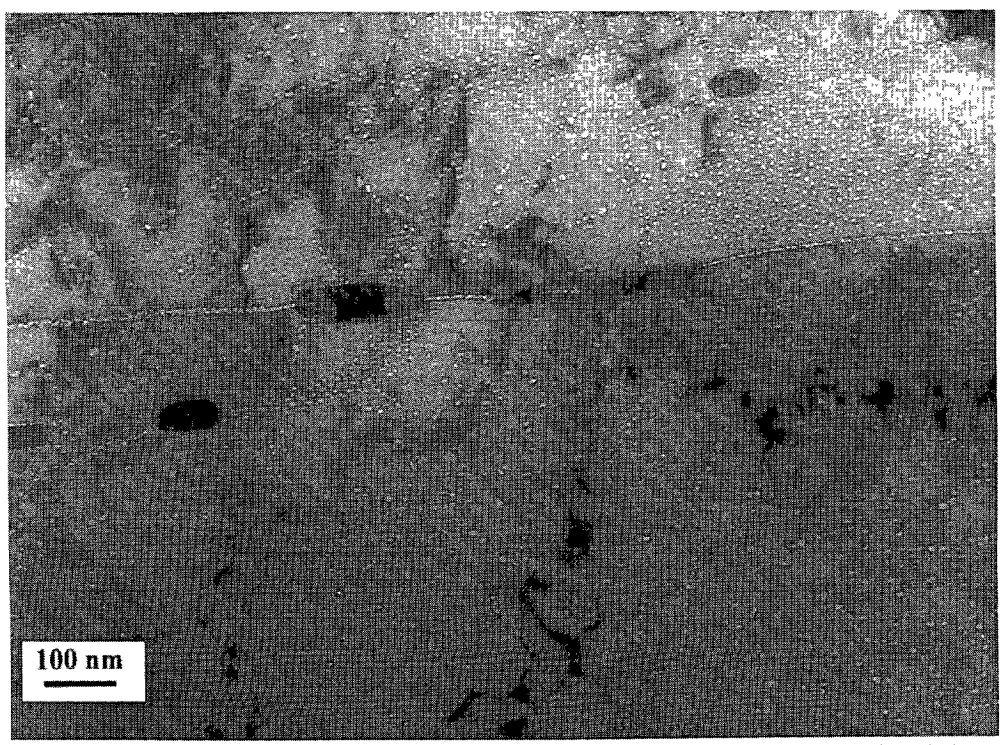

Figure 16. TEM micrograph showing the bubble microstructure in EM10 implanted with 0.5 at% He at 550°C Under-focus imaging conditions (δf = - 1000 nm).

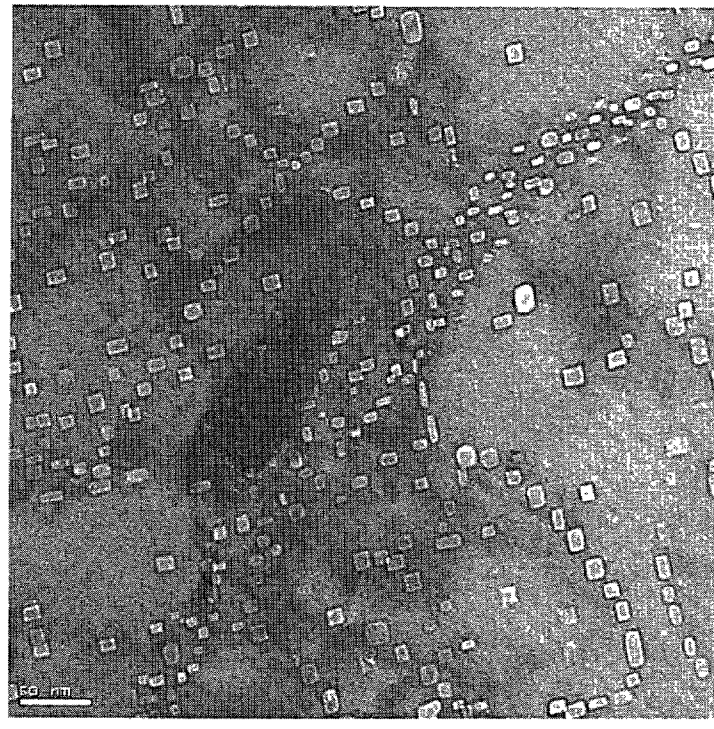

Figure 17. TEM micrograph showing faceted bubbles in EM10 implanted at 550°C with 0.5 at% He.

4. DISCUSSION

In the following, the possible causes for the observed hardening and embrittlement of He implanted EM10 and T91 steels will be discussed. We will focus on the tensile properties measured following implantation at 250°C. To our knowledge, a fully brittle intergranular fracture mode has never been reported before for conventional 9Cr martensitic steels tensile-tested at room temperature

The implantation process creates displacement damage, which amounts to approximately 0.7 dpa in the EM10 and T91 steels implanted to 0.5 at% He (cf § 2.2). To what extent does implantation-induced displacement damage contribute to the measured hardening? In order to address this question, we have plotted in *figure 18* the change in yield stress of EM10 and T91 steels implanted to 0.5 at% He or neutron irradiated at low temperature in various mixed-spectrum reactors as a function of displacement damage. In the latter case, the He production rate is very low (a few appm/dpa at most) Of course, since microstructural evolution and hence hardening of metallic materials depend on the irradiation temperature, it would have been preferable to plot data pertaining to steels irradiated at 250°C, had they been available. We want to point out, however, that one data point (T91 irradiated in the Japanese reactor JMTR [8]) corresponds to a nominal irradiation temperature virtually equal to the implantation temperature Moreover, even though the other two irradiation temperatures are either slightly lower or higher than 250°C, all data points corresponding to neutron irradiated specimens seem to follow a common trend.

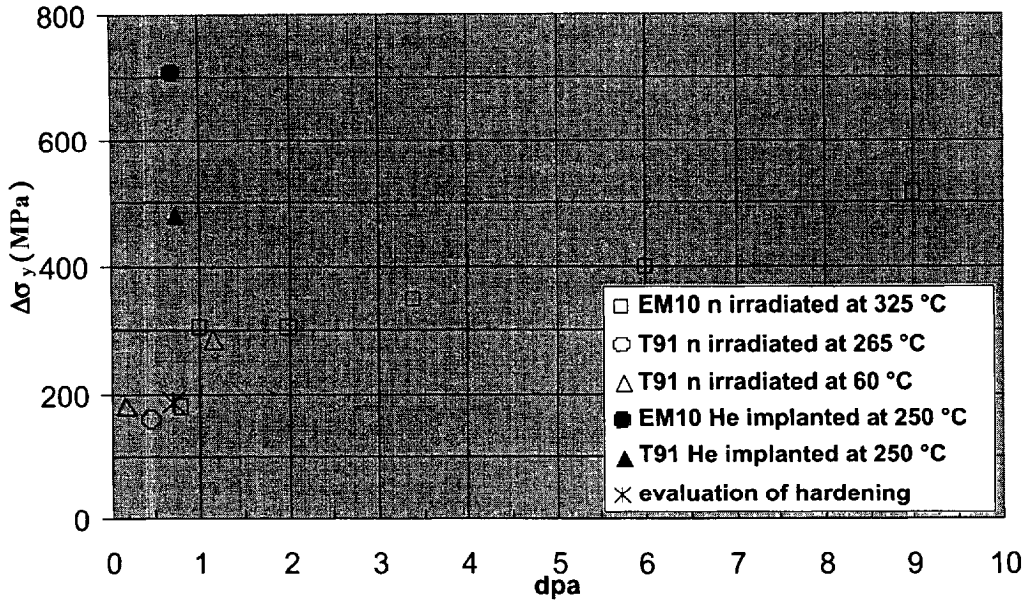

Figure 18. Evolution of the yield stress increase as a function of displacement damage The closed symbols refer to the EM10 and T91 specimens implanted to 0 5 at % He at 250°C (this work). The open symbols refer to specimens irradiated in different mixed-spectrum reactors. Circle : T91 specimen irradiated in JMTR [8], Triangles : T91 specimens irradiated in HFIR [9]. Squares : EM10 samples irradiated in OSIRIS [11, 20]. Note that all materials were in the standard tempered conditions before implantation/irradiation. Star · evaluation of hardening based on TEM microstructural data (see text for detailed explanations).

In addition to experimental results, we have also plotted in *figure 18* the change in yield strength associated with the point defect clusters (black dot damage) detected by TEM in the EM10 and T91 specimens implanted at 250°C The value of the yield stress increase $\Delta\sigma_y$ was calculated in accordance with the standard dispersed barrier hardening model (see for instance [12, 13]) using equation (1) :

$$\Delta\sigma_y = M\,\alpha\,\mu\,b\,(Nd)^{1/2} \qquad (1)$$

where μ is the shear modulus of the steel, b is the Burgers vector of the moving dislocation, α is the obstacle strength of small defect clusters, M is the averaged Taylor factor for a bcc polycristal in tension ($M \approx 3$ [14]), N is the number density of the obstacles and d their average diameter. We have assumed the following values for the different parameters : $\mu = 8\ 10^4$ MPa, $\alpha = 0.4$, b = 0.2 nm, N = 2.5 10^{22} m^{-3} and d = 3.7 nm. The values for N and d result from preliminary size and density measurements performed on TEM micrographs. The calculated value ($\Delta\sigma_y \approx 190$ MPa) follows rather well the data trend for the change in yield strength as a function of irradiation dose. However, it is obvious that the data points corresponding to the implanted samples are far above the trend. The main conclusion that can be drawn from this analysis, is that displacement induced microstructure (i.e. point defect clusters) cannot be the main cause of the very high degree of hardening displayed by the martensitic steels implanted at 250°C to 0.5 at % He.

Hunn et al. [15] came to the same conclusion (i e. that hardening in He implanted steel specimens cannot be explained by displacement damage alone), based on nanohardness measurements performed on type 316 LN austenitic stainless steel specimens irradiated at 200 °C with either 360 keV He or 3.5 MeV Fe ions. These authors found that He-induced hardening increases far more rapidly as a function of irradiation dose than is the case for the specimens irradiated with Fe ions. This behaviour however was observed only above a threshold concentration equal to approximately 1 at% He. The additional hardening in the He implanted specimens was attributed to the presence of a high number density of small He bubbles. Indeed bubble-like features could be detected by TEM above 1 at% He and were clearly imaged above 5 at%.

As mentioned in § 3.3, we were not able to detect He bubbles in the samples implanted at 250°C to 0.5 at% He. However, this does by no means exclude the possible presence of small bubbles in our He-injected specimens. Indeed, in addition to tensile samples, EM10 and T91 ribbon shaped specimens (10 mm x 10 mm, 100 μm in thickness), were implanted at the same temperature and to identical He concentrations. Following implantation, Small Angle Neutron Scattering (SANS) experiments were performed on the He containing specimens as well as on unimplanted reference samples. A preliminary analysis of the scattering spectra indicates that small bubbles did form during implantation, with a mean radius of less than 1 nm. A more detailed analysis of the SANS data will be carried out [16] and should allow to determine much more precisely the mean bubble radius as well as the bubble size distribution and number density. Nevertheless, given the He content and mean bubble size, the bubble number density is certainly very high (a rough estimate yields a number density in the $10^{24}/m^3$ range) and as a result, these bubbles are most probably the main cause for the dramatic hardening displayed by the EM10 and T91 samples implanted at 250°C to 5000 appm.

This concentration is half the threshold value above which, as mentioned above, a specific He induced hardening was measured by Hunn et al. A probable reason for this apparent discrepancy is not related to the different steels used in both studies, but rather to different implantation conditions. The implantation temperature was slighted lower in the experiments performed by Hunn et al. (200 °C) and the He injection rate (2 at ppm/s) was 2 orders of magnitude higher than that used in our experiments. Due to its extremely low solubility, He tends to form clusters when introduced into metallic materials. For a given He content and implantation temperature, He clusters will decrease in size and increase in number density as the injection rate increases. It may well be that He clusters formed during implantation at 2 at ppm/s to 0.5 at% are too small to impede significantly dislocation motion whereas larger He bubbles such as those detected by the SANS experiments mentioned above, are stronger obstacles to dislocation glide.

Ullmaier and Camus [1] performed tensile tests on He-implanted Manet (a 11% Cr martensitic steel) and 316L austenitic steel specimens. Experimental conditions (injection rate, total He content) were identical to those used in the experiments described here. However the implantation temperature was lower (between room temperature and 70 °C). Based on the comparison with other data on Manet steel irradiated in different radiation environments, the authors came to the conclusion that the observed increase in yield stress following implantation was due to displacement induced defects. The fact that helium did not contribute significantly to hardening was attributed to a fine dispersion in clusters containing only a few He atoms This hypothesis is consistent with the microstructural information obtained at 250°C (SANS data) since a decrease in implantation temperature from 250°C to 70°C, all other parameters being constant, will lead to a decrease in He cluster sizes.

It must be stressed that in contrast to what was observed on the specimens implanted at 250°C, all Manet and 316L specimens implanted by Ullmaier and Camus at low temperature and tested at room temperature and at 300 °C displayed fully ductile and transgranular fracture surfaces. Is this difference in fracture behaviour mainly related to a higher implantation-induced hardening in the specimens implanted at 250°C ? While this is certainly an important contributing factor, we believe that this higher hardening is not the only explanation. In the following, we present experimental evidence to support this assumption

Figure 19 shows the evolution of the yield stress as a function of dose for EM10 samples irradiated at 325°C in the experimental Osiris reactor [11, 20] or implanted to 0.5 at% He at 250°C, respectively. The same EM10 heat (chemical composition is given in *table 1*) was used in both experiments However, thermal treatement prior to implantation or neutron irradiation was not the same. The implanted sample was in the standard metallurgical condition (i.e. tempered martensite) whereas the neutron-irradiated specimens were in the as-quenched metallurgical condition. It can be seen that neutron irradiation at 325°C induced a large increase in yield stress, which reached at 6 dpa a value much higher than that measured in the case of the implanted sample. However, the specimen tested at RT following 6 dpa of exposure, still displayed significant ductility, as shown by the values of reduction of area, total elongation and uniform elongation equal to 56%, 9% and 1.2 %, respectively. While fracture surface observations have not yet been performed on the specimen irradiated to 6 dpa and tested at RT, the fracture surface appearance of the tensile sample irradiated to 3.4 dpa and tested at 325°C, whose yield stress is comparable to that of the implanted specimen, was found to be fully ductile as shown on *figure 20*

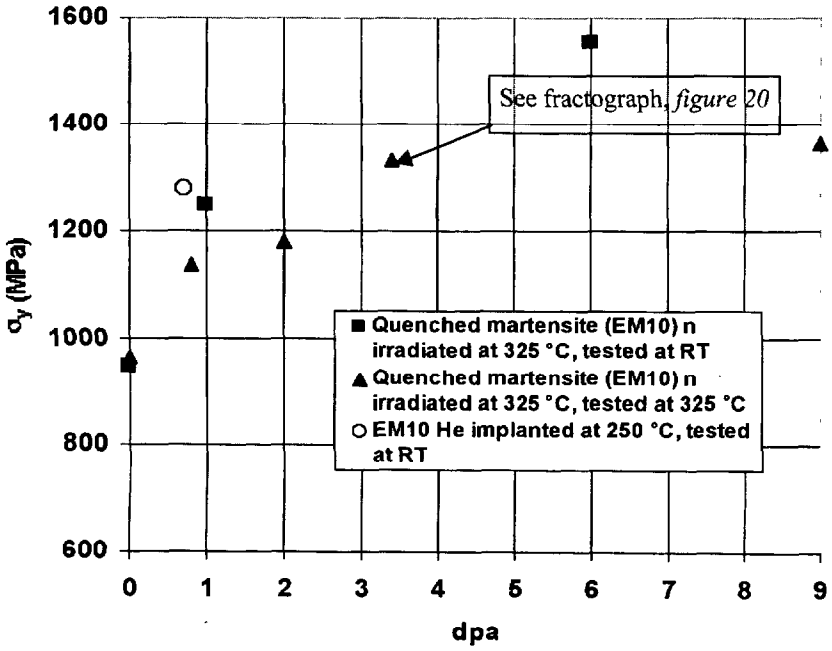

Figure 19. Evolution of the yield stress as a function of irradiation dose for EM10 samples implanted at 250°C or neutron irradiated in OSIRIS at 325°C [11, 20], respectively. See text for comments concerning the metallurgical conditions of the different specimens.

Electronic structure calculations were recently performed by Gupta [17] in order to assess the effect of He when present in iron grain boundaries. It was shown that helium induces a large reduction in grain boundary cohesion. A similar prediction was made by Smith et al [18] concerning the embrittling effect of He on nickel grain boundaries.

Therefore, it is suggested that both the high hardening of the grains following implantation at 250°C and grain boundary weakening due to helium are the two main factors leading to the observed intergranular fracture mode. The high stress values reached during the tensile tests may be sufficient to induce crack nucleation in the weakened PAG boundaries. This assumption is consistent with the fact that, for both EM10 and T91 samples implanted at 250°C and tested at RT, fracture occured in the fillet, i.e. in the region where stress concentration occurs under elastic deformation of the samples. Once nucleated the crack propagates easily along the paths provided by the embrittled PAG boundaries The presence of a high carbide density on the PAG boundaries may also promote crack nucleation and aid in the propagation of intergranular cracks, as suggested in the case of the so-called "tempered martensite embrittlement" phenomenon (see for instance [19]).

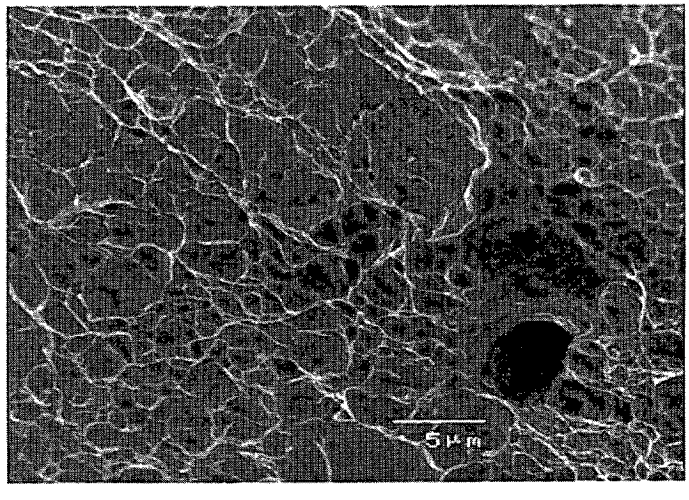

Figure 20. EM10 specimen in the as-quenched metallurgical condition, irradiated to 3.4 dpa at 325°C in OSIRIS and tested at 325°C [11, 20]. SEM micrograph showing the transgranular ductile failure mode

5. SUMMARY AND CONCLUSION

Tensile tests performed on EM10 and T91 samples implanted to 0.5 at % He at 250 and 550°C, respectively, indicated Helium–induced hardening and embrittlement, both of which are particularly severe following implantation at 250°C. Indeed, plastic deformation is totally suppressed and SEM fracture surface examinations revealed a fully brittle, predominantly intergranular fracture mode.

It was shown that the displacement-induced microstructure (black dot damage) detected by TEM in the specimens implanted at 250°C is not the main cause of the observed hardening, which is thought to be mainly due to a high density of small He bubbles. It is furthermore suggested that the brittle, intergranular fracture mode results from the conjunction of pronounced hardening and weakening of PAG boundaries due to helium.

Additional implantation experiments of martensitic steels (to lower He concentrations at 250°C and at various implantation temperatures between 250 and 550°C) coupled with microstructural investigations (SANS, TEM) will be conducted in order to obtain a more complete picture of the effects of high He concentrations on tensile properties. Investigations of the influence of He implantation rate on the He distribution would also be desirable.

A typical spallation environment is characterised by a lower He creation rate and a higher damage creation rate than in the case of the simulation experiments presented above. It is therefore expected that the helium distribution in the steels implanted at 250°C be representative of that obtained after exposure in a spallation radiation field at lower temperature. Consequently, the severe embrittlement observed after implantation at 250°C raises the question of the suitability of martensitic steels as structural materials for the ESS container window, which will operate below 250°C. The results obtained in the present study do not, however, rule out the use of 9Cr martensitic steels for the Megapie or ADS proton beam windows since in both cases the operating temperature will be significantly higher than 250°C. Nevertheless, additional data, both from simulation experiments and irradiation tests in a spallation spectrum, are obviously needed.

Acknowledgements
The contribution of H.Klein to tensile measurements and of W.Schmitz to SEM microscopy is gratefully acknowledged. This work was supported by the European Community under the SPIRE (Spallation and Irradiation Effects) project, Contract FIKW-CT-2000-00058.

6. REFERENCES

[1] H. Ullmaier and E. Camus, J. Nucl. Mater. 251 (1997) 262-268.
[2] H. Schroeder and H. Ullmaier, J. Nucl. Mater. 179-181 (1991) 118-124.
[3] G. Bauer, M. Salvatores and G. Heusener, J. Nucl. Mater. 296 (2001) 17-33.
[4] P. Jung, J. Viehweg and C. Schwaiger, Nucl. Instr. Meth. 154 (1978) 207-212.
[5] P. Jung, A. Schwarz and H.K. Sahu, Nucl. Instr. Meth. Phys. Res. A 234 (1985) 331-334.
[6] Z. He and P. Jung, Nucl. Instr. Meth. Phys. Res. B 166-167 (2000) 165-170.
[7] J. Chen and P. Jung, Report KFA Jülich, Jül-2822 (1993) ISSN 0944-2952.
[8] F. Abe, M. Narui and H. Kayano, Mater. Trans., JIM 34 (1993) 1053-1060.
[9] K. Farrell, T.S. Byun, J. Nucl Mater. 296 (2001) 129-138.
[10] F. A. McClintock and A.S. Argon, Mechanical Behavior of Materials. Addison-Wesley Publishing Company, Reading, Massachussetts, U.S.A., 1966.
[11] J.C. Brachet, X. Averty, P. Lamagnère, A. Alamo, F. Rosenblum, O. Raquet and J.L. Bertin, Effects of Radiation on Materials : 20th International Symposium, ASTM STP 1405, S.T. Rosinski, M.L. Grossbeck, T.R. Allen and A S. Kumar, Eds., ASTM, West Conshohocken, PA (2001) 500-520.
[12] A J. Ardell, Met. Trans. A 16 (1985) 2131-2165.
[13] G.E. Lucas, J. Nucl Mater. 206 (1993) 287-305.
[14] U.F. Kocks, Met. Trans. 1 (1970) 1121-1143.
[15] J.D. Hunn, E.H. Lee, T.S. Byun and L.K. Mansur, J. Nucl. Mater. 282 (2000) 131-136.
[16] J. Henry, M-H. Mathon, P. Jung, to be published.
[17] R. Gupta (CEA-SRMP), to be published.
[18] R.W. Smith, W.T. Geng, C B. Geller, R. Wu and A.J. Freeman, Scripta mater. 43 (2000) 957-961.
[19] C.L. Briant, Mater. Sci. Technol. 5 (1989) 138-147.
[20] X. Averty, O. Rabouille, J.J. Espinasse (CEA-SEMI), to be published.
[21] J.F. Ziegler, J.P. Biersack, U. Littmark, The Stopping and Ranges of Ions in Solids, Pergamon Press, New York (1996).